Scientific Research Publishing

International Journal of Astronomy and Astrophysics, 2023, 13, 1-24
https://www.scirp.org/journal/ijaa
ISSN Online: 2161-4725
ISSN Print: 2161-4717

Transport in Astrophysics: III. Diffusion from the Galactic Plane

Lorenzo Zaninetti

Physics Department, University of Turin, Turin, Italy
Email: l.zaninetti@alice.it

How to cite this paper: Zaninetti, L. (2023) Transport in Astrophysics: III. Diffusion from the Galactic Plane. *International Journal of Astronomy and Astrophysics*, **13**, 1-24.
https://doi.org/10.4236/ijaa.2023.131001

Received: December 21, 2022
Accepted: March 17, 2023
Published: March 20, 2023

Abstract

New solutions, for the stationary and temporary states, are derived for the 1D diffusion of cosmic rays in the presence of losses. The new results are applied to the latitude profile of radiation emitted above the galactic plane. Percolation theory for a spiral galaxy coupled with the evolution of the super-bubbles allows building a model for the radiation of a spiral galaxy as seen face on. The annulus of radiation of our galaxy is also simulated and the excess of radiation observed at the centre of our galaxy is explained by the sine law which arises in the theory of the image.

Keywords

Particle Diffusion, Galaxy: Centre, Galaxy: Disk

1. Introduction

We now analyse, in chronological order, some topics raised by the connection between the acceleration/diffusion/confinement of cosmic rays (CR) and super-bubbles/super-shells (SB): the CR confinement from SBs means that the mean age would be independent of energy [1], the constancy of CR-produced Be relative to supernova-produced Fe observed in halo stars formed in the early Galaxy [2], a model for the observations of the evolution of ^{6}LiBeB [3], an explanation for the well-known anomalous ^{22}Ne/^{20}Ne ratio [4], the acceleration of cosmic-ray nuclei heavier than He in enriched SB interiors [5], production of CR by supra-thermal ion injection [6], a discussion of the fraction of the unaccounted for energy which is converted in CR [7], an investigation of the shape of the spectrum of high-energy protons produced inside the SB blown around clusters of massive stars [8], a model based on two coupled stochastic differential equations, which is applied to protons and alpha particles [9], a discussion of the non-thermal

spectrum between 1.5 and 8.8 GHz which is fitted with a standard model of an aging cosmic-ray electron population [10], a model which includes advection, diffusion, thermal conduction and radiative cooling for CR [11], a framework tying together the sources, injection, acceleration, and propagation of CRs [12], an evaluation of the distribution of pions from continuous losses of CR [13], analysis of the generalized Kompaneets' equations adapted to expansion in various external density profiles and coupled with escaping CRs [14], production of γ-ray radiation in the interactions between cosmic rays and interstellar gas in the Orion-Eridanus SB [15] and acceleration of particles and non-linear feedback [16]. Another point for research is the excess in γ-rays observed by the Fermi Large Area Telescope at the centre of the Galaxy, which can be explained by annihilating dark matter, [17]. The already cited papers leave a series of questions unanswered or only partially answered:

- Is it possible to model the 1D diffusion with losses in the stationary and transient cases?
- Is it possible to model a coupling between percolation theory which allows building a spiral galaxy and the evolution of the SBs in the galactic plane?
- Can the galactic latitude and longitude cuts of observed radiation be explained by the diffusion?
- Do the galactic longitude cuts of observed radiation follow the sine law?

In order to answer the above questions, Section 2 reviews the connection between random walks and diffusion, Section 3 reviews stationary diffusions with losses and introduces a new stationary diffusion with losses, Section 4 introduces the new transient diffusion with losses, and Section 5.2 applies the new results about 1D diffusion to the latitude profiles of the galactic plane for the observed radiation. Section 6 reviews a model for a spiral galaxy as given by percolation theory, introduces a simple model for the SBs, models the diffusion of CRs from the SBs and finally displays the observed radiation for a spiral as seen face on, in Mollweide projection and as longitude profiles.

2. The Random Walk

The dependence of the mean square displacement, $\overline{R^2(t)}$, according to Equation (8.38) in [18] is

$$\overline{R^2(t)} = 2dDt \quad (t \to \infty), \tag{1}$$

where d is the number of spatial dimensions. From Equation (1), the diffusion coefficient is derived in the continuum:

$$D = (t \to \infty)\frac{\overline{R}^2}{2dt}. \tag{2}$$

Using discrete time steps, the average square radius after N steps, Equation (12.5) in [18], is

$$\left\langle R^2(N) \right\rangle \sim 2dDN, \tag{3}$$

from which the diffusion coefficient is derived:

$$D = \frac{\left\langle R^2(N) \right\rangle}{2dN}. \tag{4}$$

If $\left\langle R^2(N) \right\rangle \sim N$, the diffusion coefficient is

$$D = \frac{1}{2d} \lambda v_{tr} \tag{5}$$

when the step length of the walker or mean free path between successive collisions is λ and the transport velocity is v_{tr}. The above formula allows an astrophysical evaluation of the diffusion coefficient. The mean free path is here chosen to be the gyro-radius of the relativistic ions, ρ_Z. Once the energy is expressed in units of 10^{15} eV (E_{15}), and the magnetic field in 10^{-6} Gauss (H_{-6}) we have

$$\rho_Z = 1.08 \frac{E_{15}}{H_{-6} Z} \text{ pc}, \tag{6}$$

where Z is the atomic number. On assuming that the CRs diffuse with a mean free path equal to the relativistic gyro-radius, the transport velocity is equal to the speed of light and $d = 1$, the case here analysed, the diffusion coefficient according to Equation (5), is

$$D = \frac{0.1654 E_{15}}{Z B_{-6}} \frac{\text{pc}^2}{\text{year}} = \frac{1.654 \times 10^{-7} E_{GeV}}{Z B_{-6}} \frac{\text{pc}^2}{\text{year}}. \tag{7}$$

3. The Stationary Diffusion

We now analyse the stationary 1D diffusion both in the absence and presence of losses. In the following, spatial distance is expressed in pc, the time in years, and the diffusion coefficient in $\frac{\text{pc}^2}{\text{yr}}$.

3.1. Absence of Losses

Fick's second law in 1D states that a change in concentration, $u(x,t)$, in any part of the system is due to an inflow and an outflow of material into and out of a part of the system:

$$\frac{\partial}{\partial t} u(x,t) = D\left(\frac{\partial^2}{\partial x^2} u(x,t) \right), \tag{8}$$

where D is the diffusion coefficient and t is the time. For a stationary state, the above equation is

$$D\left(\frac{\partial^2}{\partial x^2} u(x,t) \right) = 0. \tag{9}$$

The concentration increases from 0 at $x = a$ to a maximum value C_m at $x = b$ and then falls again to 0 at $x = c$. The two solutions are

$$u(x) = \frac{C_m (a - x)}{a - b} \quad a < x < b, \tag{10}$$

and

$$u(x) = -\frac{C_m(c-x)}{b-c} \quad b < x < c. \tag{11}$$

3.2. Presence of Losses

The presence of losses modifies Fick's second law in 1D for the steady state, see Equation (8) as

$$D\left(\frac{\mathrm{d}^2}{\mathrm{d}x^2}u(x)\right) - a_l u(x) = 0, \tag{12}$$

where the parameter a_l regulates the losses and is expressed in $\frac{1}{\text{year}}$. The concentration increases from 0 at $x = a$ to a maximum value C_m at $x = b$ and then falls again to 0 at $x = c$. The two solutions are

$$u(x) = \frac{C_m\left(\mathrm{e}^{\frac{\sqrt{a_l}(2a-b-x)}{\sqrt{D}}} - \mathrm{e}^{-\frac{\sqrt{a_l}(b-x)}{\sqrt{D}}}\right)}{\mathrm{e}^{\frac{2\sqrt{a_l}(a-b)}{\sqrt{D}}} - 1}; \quad a < x < b, \tag{13}$$

and

$$u(x) = \frac{\left(-\mathrm{e}^{\frac{\sqrt{a_l}(b-x)}{\sqrt{D}}} + \mathrm{e}^{\frac{\sqrt{a_l}(b-2c+x)}{\sqrt{D}}}\right)C_m}{\mathrm{e}^{\frac{2\sqrt{a_l}(b-c)}{\sqrt{D}}} - 1}; \quad b < x < c. \tag{14}$$

The solution with $a < x < b$ is reported in Appendix A. Figure 1 reports the new 1D theoretical solution when the coefficient of the losses is variable.

4. The Transient Diffusion with Losses

Fick's second law in 1D in the presence of losses states that a change in concentration, $u(x,t)$, is

$$\frac{\partial}{\partial t}u(x,t) = D\left(\frac{\partial^2}{\partial x^2}u(x,t)\right) - a_l u(x,t), \tag{15}$$

where D is the diffusion coefficient, t is the time and the parameter a_l regulates the losses. We now solve Fick's second law in 1D over the spatial domain $[0,L]$ in the presence of an initial profile (the initial condition) for the number of particles. The *first* case to be analysed is an initial exponential profile of concentration

$$N(x,0) = N_0 \mathrm{e}^{-\frac{xs}{L}}, \tag{16}$$

where s is an adjustable parameter and N_0 the number of particles at $x = 0$. The boundary conditions are assumed to be $\frac{\partial}{\partial x}u(0,t) = 0$, $\frac{\partial}{\partial x}u(L,t) = 0$ and the solution is the following Fourier series

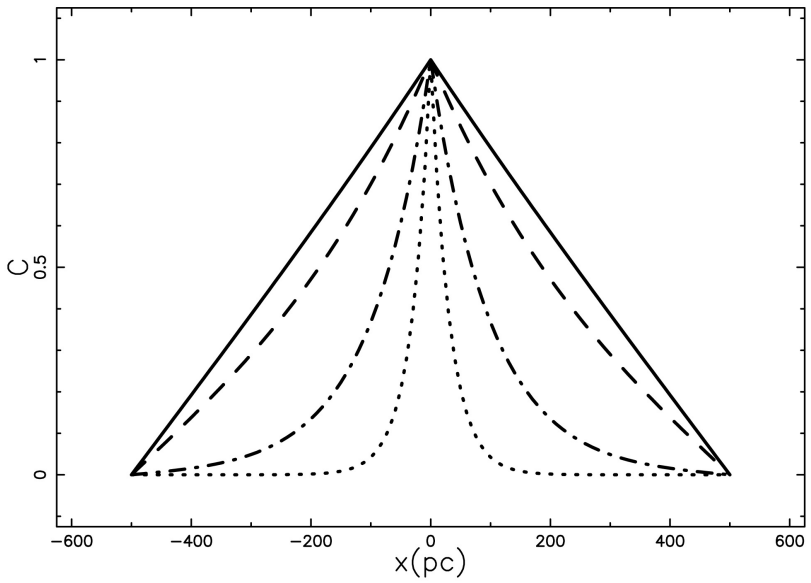

Figure 1. Values of concentration in the case of steady state with losses computed with Equations (13) and (14) when $a=-500$ pc, $b=0$ pc, $c=500$ pc and $D=1\frac{\mathrm{pc}^2}{\mathrm{yr}}$: $a_l=1.0\times10^{-6}\frac{1}{\text{year}}$ (full line), $a_l=1.0\times10^{-5}\frac{1}{\text{year}}$ (dashed), $a_l=1.0\times10^{-4}\frac{1}{\text{year}}$ (dot-dash-dot-dash), $a_l=1.0\times10^{-3}\frac{1}{\text{year}}$ (dotted).

$$u(x,t)=\frac{1}{s}\left(-N_0\mathrm{e}^{-a_l t}\mathrm{e}^{-s}+N_0\mathrm{e}^{-a_l t}+\left(\sum_{n=1}^{\infty}\left(-\frac{2\cos\left(\frac{n\pi x}{L}\right)\mathrm{e}^{-\frac{t\left(D\pi^2n^2+L^2a_l\right)}{L^2}}sN_0\left(\mathrm{e}^{-s}(-1)^n-1\right)}{\pi^2n^2+s^2}\right)\right)s\right). \quad (17)$$

A 3D surface of the solution as a function of space and time is reported in **Figure 2**. The *second* case to be analysed is an initial sine profile for the concentration,

$$N(x,0)=N_0\sin\left(\frac{\pi x}{L}\right) \quad (18)$$

where N_0 is the number of particles at $x=0$. The boundary conditions are assumed to be $\frac{\partial}{\partial x}u(0,t)=0$, $\frac{\partial}{\partial x}u(L,t)=0$ and the solution is the following Fourier series

$$u(x,t)=\frac{2N_0\mathrm{e}^{-a_l t}}{\pi}+\sum_{n=2}^{\infty}\left(-\frac{2\cos\left(\frac{n\pi x}{L}\right)\mathrm{e}^{-\frac{t\left(D\pi^2n^2+L^2a_l\right)}{L^2}}N_0\left((-1)^n+1\right)}{\pi\left(n^2-1\right)}\right). \quad (19)$$

The solution as a function of x and t is presented as a surface plot in **Figure 3**.

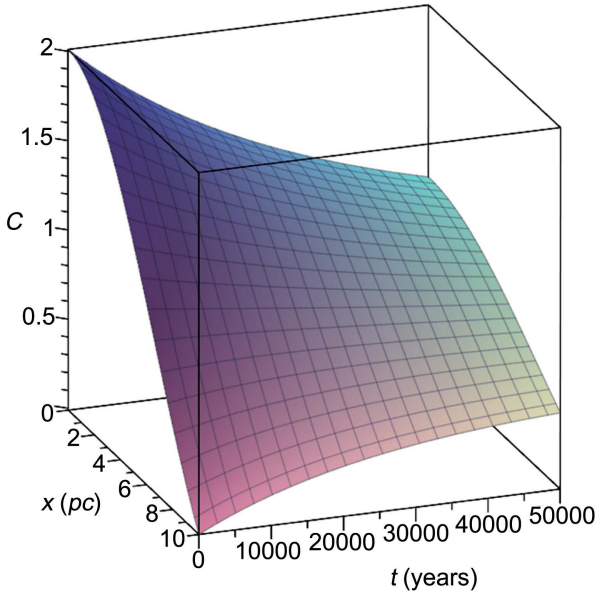

Figure 2. Values of concentration in the transient case with losses in the presence of an exponential profile as computed with Equation (17) as a function of space and time when L = 1000 pc, $D = 5 \times 10^{-4} \frac{\text{pc}^2}{\text{yr}}$, $s = 1.0 \times 10^{-5}$. $N_0 = 1.0 \times 10^3$ and $a_l = 1.0 \times 10^{-3} \frac{1}{\text{year}}$.

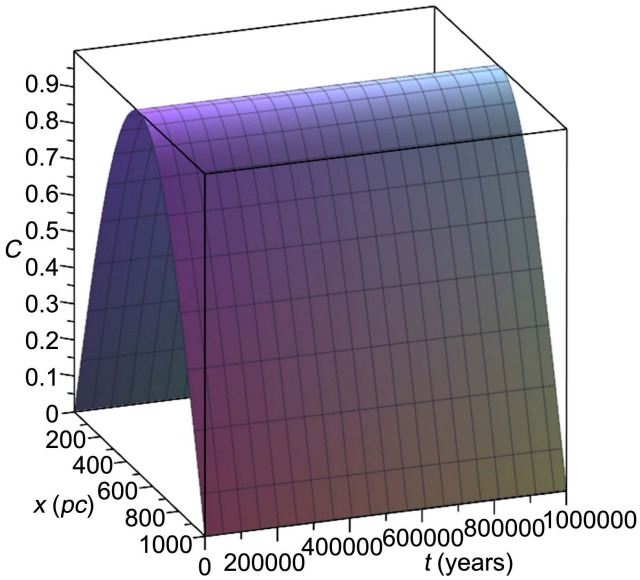

Figure 3. Values of concentration in the transient case with losses in the presence of a sine profile as computed with Equation (19) as a function of space and time when L = 1000 pc, $D = 1 \times 10^{-6} \frac{\text{pc}^2}{\text{yr}}$, $N_0 = 1.0$ and $a_l = 1.0 \times 10^{-10} \frac{1}{\text{year}}$.

An example of the influence of the parameter a_l on the solution is reported in **Figure 4**. The *third* case is an initial $\sin^4$ profile for the concentration

$$N(x,0) = N_0 \left(\sin^4 \left(\frac{\pi x}{L} \right) \right) \tag{20}$$

where N_0 the number of particles at $x=0$. The boundary conditions are assumed to be $\frac{\partial}{\partial x}u(0,t)=0$, $\frac{\partial}{\partial x}u(L,t)=0$ and the analytical solution is

$$u(x,t)=\frac{N_0\left(\cos\left(\frac{4\pi x}{L}\right)e^{-\frac{t\left(16D\pi^2+L^2a_l\right)}{L^2}}-4\cos\left(\frac{2\pi x}{L}\right)e^{-\frac{t\left(4D\pi^2+L^2a_l\right)}{L^2}}+3e^{-a_l t}\right)}{8}. \quad (21)$$

The solution as a function of time and space is reported in Figure 5.

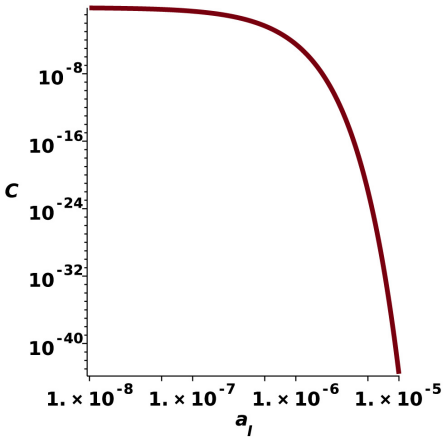

Figure 4. Values of concentration in the transient case with losses in the presence of a sine profile as a function of a_l when L = 1000 pc, x = 250 pc, $D=1\times10^{-6}\frac{\text{pc}^2}{\text{yr}}$ and $N_0=1.0$.

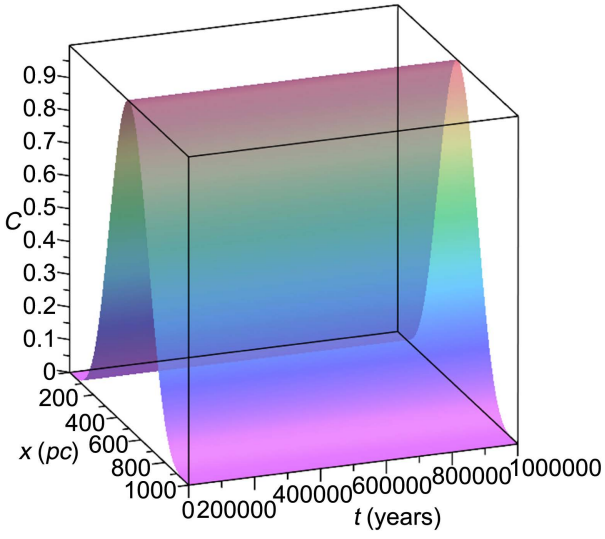

Figure 5. Values of concentration with losses in the presence of a $\sin^4$ profile computed with Equation (21) as function of space and time when L = 1000 pc, $D=1\times10^{-6}\frac{\text{pc}^2}{\text{yr}}$, $N_0=1.0$ and $a_l=1.0\times10^{-10}\frac{1}{\text{year}}$.

5. Astrophysical Profiles

5.1. Statistics

The merit function χ^2 is computed according to the formula

$$\chi^2 = \sum_{i=1}^{n} \frac{(T_i - O_i)^2}{O_i}, \tag{22}$$

where n is the number of elements of the sample, T_i is the theoretical value, and O_i is the experimental data. In the following we will compare our results with two standard types of fits. The *first* is the polynomial fit of degree m

$$y(x) = a_0 + a_1 x + a_2 x^2 + \cdots + a_m x^m, \tag{23}$$

where the a_1 are $m+1$ unknown coefficients, see the Fortran subroutine lfit in [19]. The second *fit* is represented by the Gaussian function

$$y(x) = \frac{C e^{\frac{(x-x_m)^2}{2\sigma^2}} \sqrt{2}}{2\sqrt{\pi}\sigma}, \tag{24}$$

where C, x_m and σ are three parameters to be found with the Levenberg method, see the Fortran subroutine mrqmin in [19].

5.2. Latitude Profile

Astronomers usually report the intensity of emission in the various bands as flux versus galactic latitude or galactic longitude. In the following we will assume that the synchrotron radiation which is thought to vary from the radio to the γ region is proportional to the concentration of the diffusing CR. Further, the distance from the galactic plane, the vertical galactic height, is assumed to be proportional to the galactic latitude. We now make a comparison between the observed flux versus the galactic latitude and the theoretical behaviour of the concentration of CR as given by the diffusion. A *first* example is given by the γ-ray diffuse emission around 15 TeV as reported in **Figure 3** in [20]. **Figure 6** reports the observed data and the model of 1D diffusion with an exponential profile of concentration, χ^2 of the various models in **Table 1**.

A *second* example is given by the γ-ray diffuse emission as detected by AR-GO-YBJ in the interval [350 GeV, 2 TeV] which is reported in Figure 2 of [21]. **Figure 7** reports the observed data and the model of 1D diffusion with a sine profile of concentration, χ^2 of the various models in **Table 1**.

Table 1. Numerical values of the parameters for the χ^2 as given by Equation (22) for different profiles and different models.

Model	Reference	χ^2, Model	χ^2, Polynomial profile	χ^2, Gaussian profile
exponential profile	[20]	25.35	18.5	5.1
sine profile	[21]	45.27	17.97	7.25
stationary 1D	[22]	176,747	931,530	337,555

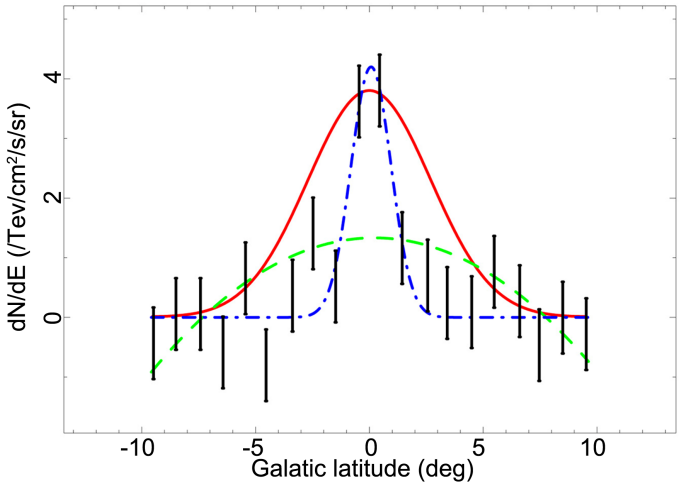

Figure 6. The γ-ray flux as reported in Figure 3 of [20], inner Galaxy or $30 < l < 65$, is displayed as black points with error bar. The red full line reports the values of concentration computed with 1D diffusion in the presence of an exponential profile, see Equation (17), when $L = 1000$ pc, $D = 4 \times 10^{-3} \frac{\text{pc}^2}{\text{yr}}$, $t = 10^7$ years, $s = 10^5$, $N_0 = 1$ and $a_l = 10^{-6} \frac{1}{\text{year}}$. The green dashed line represents the polynomial approximation and the blue dash-dot-dash the Gaussian approximation.

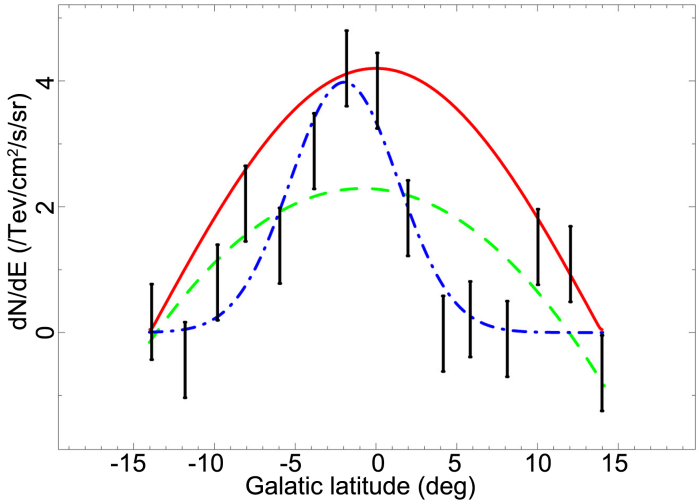

Figure 7. The γ-ray flux as reported in Figure 2 of [21] is displayed as black points with error bar. The red full line reports the values of concentration computed with 1D diffusion in the presence of a sine profile, see Equation (19), when $L = 1000$ pc, $D = 10^{-6} \frac{\text{pc}^2}{\text{yr}}$, $t = 10^7$ years, $N_0 = 1$ and $a_l = 10^{-10} \frac{1}{\text{year}}$. The green dashed line represents the polynomial approximation and the blue dash-dot-dash the Gaussian approximation.

A *third* example is given by the radio emission at 408 MHz as detected by Planck which is reported in Figure 4 of [22]. **Figure 8** reports the observed data and the model of 1D stationary diffusion with losses, χ^2 of the various models in **Table 1**.

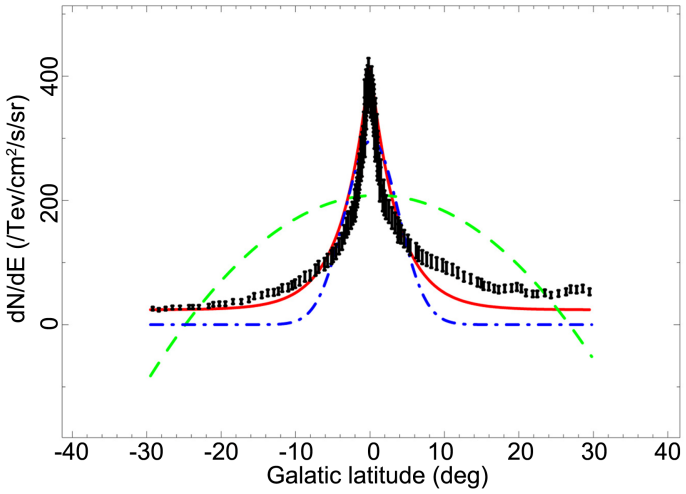

Figure 8. The radio flux at 408 MHz as reported in Figure 4 of [22] is displayed as black points with error bar. The red full line reports the values of concentration computed with 1D stationary diffusion with losses, see Equations (13) and (14), when L = 1000 pc, $D = 1\frac{\text{pc}^2}{\text{yr}}$, $C_m = 1$ and $a_l = 2.5\times10^{-4}\frac{1}{\text{year}}$. The green dashed line represents the polynomial approximation and the blue dash-dot-dash the Gaussian approximation.

6. The Diffusion in a Spiral Galaxy

We now review percolation theory, a model for the evolution of SBs, the diffusion from many injection points, some elements of the theory of the image which allows building theoretical profiles of the intensity of radiation versus galactic longitude, and an evaluation for the index of galactic CRs.

6.1. Percolation

The appearance of arms can be simulated through percolation theory [23]-[28]. The fundamental hypotheses and the parameters adopted in the simulation are now reviewed.

1) The motion of a gas on the galactic plane has a constant rotational velocity, denoted by V_G (in the case of spiral type Sb 218 km·s^{-1}). Here the velocity, V_G, is expressed in units of 200 km·s^{-1} and will therefore be V_G = 1.39.

2) The polar simulation array made by rings and cells has a radius R_G = 12 kpc. The number of rings, (59), by the multiplication of R_G with the number of rings for each kpc, denoted by nring/kpc, which in our case is 5. Every ring is then made up of many *cells*, each one with a size on the order of the galactic thickness, ≈0.2 kpc. The parameter nring/kpc can also be found by dividing 1 kpc by the cell's approximate size.

3) The global number of cells, 11,121, multiplied by the probability of the spontaneous formation of a new cluster, p_{sp} (for example 0.01), allows the process to start (with the previous parameters, 111 new clusters were generated). Each one of these sources has 6 new surroundings that are labeled for each ring.

4) In order to better simulate the decrease of the gas density along the radius, a stimulated probability of forming new clusters with a linear dependence by the

radius, $p_{st} = a + bR$, was chosen. The values a and b are found by fixing *prmax* (for example 0.18), the stimulated probability at the outer ring, and *prmin* (for example 0.24) in the inner ring; of course, $prmin \geq prmax$. This approach is surprisingly similar to the introduction of an anisotropic probability distribution in order to better simulate certain classes of spirals [29].

5) Now, new sources are selected in each ring based on the hypothesis of different stimulated probabilities. A rotation curve is imposed so that the array rotates in the same manner as the galaxy. The procedure repeats itself n times (100); we denote by t_G the age of the simulation, viz., 100×10^7 yr, where 10^7 yr is the astrophysical counterpart of one time step.

6) In order to prevent catastrophic growth, the process is stopped when the number of surroundings is greater than *max* (1000) and restarts by spontaneous probability.

7) The final number of active cells (3824) is plotted with the size, which decreases linearly with the age of the cluster. In other words, the young clusters are bigger than the old ones. Only 10 cluster ages are shown; only cells with an age of less than life (in our case 10×10^7 yr) are selected.

A typical run is shown in Figure 9 and in Table 2 we summarize the parameters used in this simulation.

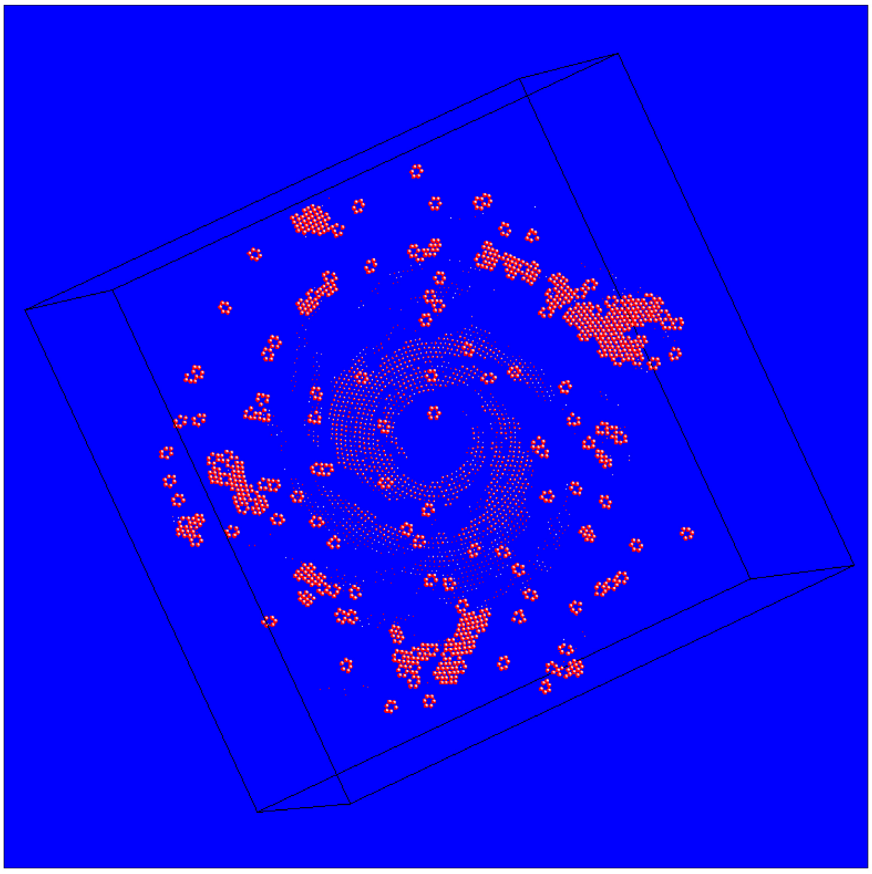

Figure 9. A typical simulation of the galaxy's arms with the parameters as in Table 2 and radius of a cluster inversely proportional to its lifetime.

Table 2. Parameters of the model.

Galactic radius	12 kpc
Rings/kpc	5
Stochastic probability	0.01
Timestep	10^7 years
Cells	11,121
Active	3894

A discussion of the location of the spiral arms and that of the peak of the total synchrotron emission can be found in [30].

6.2. The Density Profile

The vertical density distribution of galactic H I is well-known; specifically, it has the following three component behavior as a function of z, the distance from the galactic plane in pc:

$$n\left(z;n_1,n_2,n_3,H_1,H_2,H_3\right)=n_1\mathrm{e}^{-z^2/H_1^2}+n_2\mathrm{e}^{-z^2/H_2^2}+n_3\mathrm{e}^{-|z|/H_3}. \tag{25}$$

We took [31] [32] [33] $n_1=0.395$ particles cm^{-3}, $H_1=127$ pc, $n_2=0.107$ particles cm^{-3}, $H_2=318$ pc, $n_3=0.064$ particles cm^{-3}, and $H_3=403$ pc. This distribution of galactic H I is valid in the range $0.4\le R\le R_0$, where $R_0=8.5$ kpc and R is the distance from the galactic centre. We now fit the above profile with the following theoretical inverse square dependence on z, n_{th}, in Cartesian coordinates,

$$n_{th}\left(z;z_0,n_0\right)=n_0\left(1+\frac{z}{z_0}\right)^{-2}, \tag{26}$$

where n_0 is the number density of the three component medium at $z=0$ and z_0 can be found by minimizing the χ^2 of the difference of the two functions (**Figure 10**).

6.3. The Super-Bubbles

In spherical coordinates the density is assumed to be

$$\rho\left(z;z_0,\rho_0,\theta\right)=\begin{cases}\rho_0 & r<r_0\\ \dfrac{\rho_0}{\left(1+\dfrac{r\cos(\theta)}{z_0}\right)^2} & r_0<r\end{cases} \tag{27}$$

where the parameter z_0 fixes the scale, ρ_0 is the density at $z=z_0$, and θ is the polar angle. Given a solid angle $\Delta\Omega$, the mass M_0 swept in the interval $\left[0,r_0\right]$ is

$$M_0=\frac{1}{3}\rho_0 r_0^3\Delta\Omega. \tag{28}$$

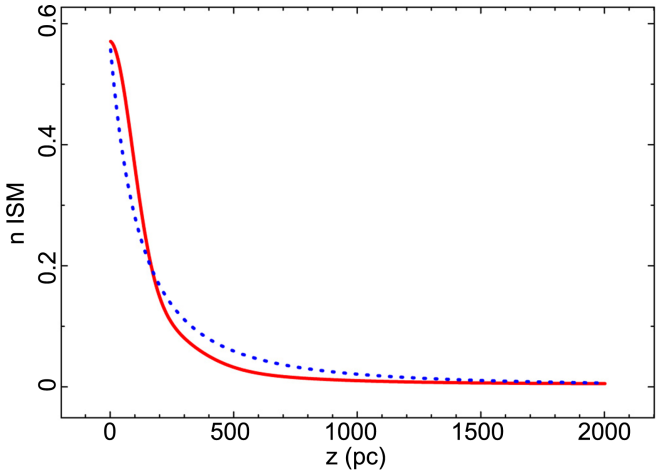

Figure 10. Profiles of density versus scale height z: the inverse square profile given by Equation (26) when $z_0 = 239$ pc, and $n_0 = 0.565$ particles cm^{-3}, (blue dotted line) and the three-component exponential distribution as given by Equation (25) (red full line).

The total mass swept, $M\left(r; r_0, z_0, \theta, \rho_0, \Delta\Omega\right)$, in the interval $[0, r]$ is

$$\begin{aligned} & M\left(r; r_0, z_0, \theta, \rho_0, \Delta\Omega\right) \\ & = \left(\frac{1}{3}\rho_0 r_0^3 + \frac{\rho_0 z_0^2 r}{\left(\cos(\theta)\right)^2} - 2\frac{\rho_0 z_0^3 \ln\left(r\cos(\theta)+z_0\right)}{\left(\cos(\theta)\right)^3} \right. \\ & - \frac{\rho_0 z_0^4}{\left(\cos(\theta)\right)^3\left(r\cos(\theta)+z_0\right)} - \frac{\rho_0 z_0^2 r_0}{\left(\cos(\theta)\right)^2} + 2\frac{\rho_0 z_0^3 \ln\left(r_0\cos(\theta)+z_0\right)}{\left(\cos(\theta)\right)^3} \\ & \left. + \frac{\rho_0 z_0^4}{\left(\cos(\theta)\right)^3\left(r_0\cos(\theta)+z_0\right)} \right) \Delta\Omega. \end{aligned} \tag{29}$$

The differential equation which models the conservation of momentum is

$$\begin{aligned} & \left(\frac{1}{3}\rho_0 r_0^3 + \frac{\rho_0 z_0^2 r(t)}{\left(\cos(\theta)\right)^2} - 2\frac{\rho_0 z_0^3 \ln\left(r(t)\cos(\theta)+z_0\right)}{\left(\cos(\theta)\right)^3} \right. \\ & - \frac{\rho_0 z_0^4}{\left(\cos(\theta)\right)^3\left(r(t)\cos(\theta)+z_0\right)} - \frac{\rho_0 z_0^2 r_0}{\left(\cos(\theta)\right)^2} + 2\frac{\rho_0 z_0^3 \ln\left(r_0\cos(\theta)+z_0\right)}{\left(\cos(\theta)\right)^3} \\ & \left. + \frac{\rho_0 z_0^4}{\left(\cos(\theta)\right)^3\left(r_0\cos(\theta)+z_0\right)} \right) \frac{\mathrm{d}}{\mathrm{d}t} r(tk) - \frac{1}{3}\rho_0 r_0^3 v_0 = 0, \end{aligned} \tag{30}$$

where the initial conditions are $r = r_0$ and $v = v_0$ when $t = t_0$. The adopted astrophysical units are pc for space and year for time. The starting parameters of the inverse square model are N^*, the number of SN explosions in 5.0 × 10^7 yr, E_{51}, the energy in 10^{51} erg, v_0, the initial velocity which is fixed by the bursting phase, t_0, the initial time in yr which is equal to the bursting time, and t the proper time of the SB.

A possible set of initial values is reported in **Table 3** in which the initial values of the radius and velocity are fixed by the bursting phase.

Table 3. Numerical values of the parameters for the simulation in the case of the inverse square model.

$n_0\left[\frac{\text{particles}}{\text{cm}^3}\right]$	1
E_{51}	1
N^*	5.87×10^8
r_0	220 pc
v_0	3500 km/s
z_0	239
t	5.95×10^7 yr
t_0	36,948 yr

In order to simulate the structure of the galactic plane, the same basic parameters as in Figure 9 can be chosen, but now the SBs are drawn with an equal-area Aitoff projection. In particular, a certain number of clusters will be selected through a random process according to the following formula:

$$\text{selected clusters} = \text{pselect} \cdot \text{number of clusters from percolation}, \tag{31}$$

where pselect has a probability lower than one. The final result of the simulation for the network of the SBs is reported in Figure 11.

6.4. Diffusion of CR from SB

We now model the 1D diffusion from many injection points (in the following IP) in a 3D space, disposed on N_{SB} SBs. The rules are:

1) The first of N_{SB} SB is chosen.

2) The IPs, for example 200, are randomly generated on the surface of the selected SB.

3) The values of concentration from the multiple diffusion, the IPs, are recorded on a 3D grid $\mathcal{M}(x,y,z)$ which covers the considered 3D space.

4) At each point of $\mathcal{M}(x,y,z)$ we evaluate the distance of the nearest IP

5) The value of $\mathcal{M}(x,y,z)$ is computed with Formula (A.1) in the case of a steady state diffusion with losses, see Table 4, or Formula (21) in the case of transient diffusion in the presence of an initial exponential profile of concentration, see Table 5.

6) The next SB is chosen and the process restarts from point 2.

6.5. The Image Theory

The transfer equation in the presence of emission only, see for example [34] or [35], is

$$\frac{\mathrm{d}I_\nu}{\mathrm{d}s} = -k_\nu \zeta I_\nu + j_\nu \zeta, \tag{32}$$

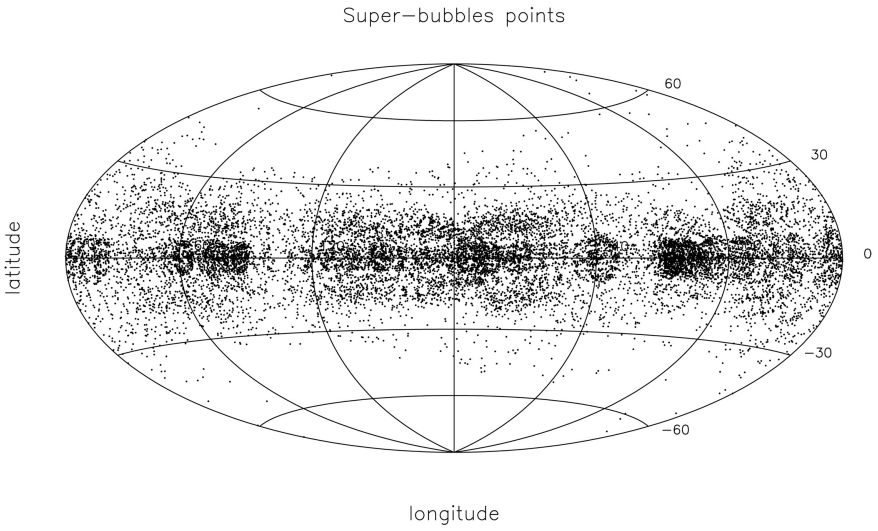

Figure 11. Structure of the galactic plane in the Hammer-Aitoff projection, as resulting from the SB/percolation network. The value of pselect is 0.04, corresponding to 143 selected clusters. The parameters of the inverse square model are reported in **Table 3** and each SB has 200 random points on its surface.

Table 4. Numerical values of the parameters for the diffusion in the case of 1D stationary diffusion with losses, see Equations (13) and (14).

$a = -1000$ pc
$b = 0$ pc
$c = 1000$ pc
$D = 10^{-4}$ pc^2/yr
$C_m = 10^2$
$a_l = 10^{-9}$/year

Table 5. Numerical values of the parameters for the diffusion in the case of transient diffusion with losses computed with Equation (21).

$L = 2000$ pc
$D = 10^{-4}$ pc^2/yr
$N_0 = 10^3$
$t = 3 \times 10^7$ year
$a_l = 10^{-10}$/year

where I_ν is the specific intensity, s is the line of sight, j_ν the emission coefficient, k_ν a mass absorption coefficient, ζ the mass density at position s, and the index ν denotes the relevant frequency of emission. The solution to Equation (32) is

$$I_\nu(\tau_\nu) = \frac{j_\nu}{k_\nu}\left(1 - e^{-\tau_\nu(s)}\right), \tag{33}$$

where τ_ν is the optical depth at frequency ν

$$d\tau_\nu = k_\nu \zeta ds. \tag{34}$$

We now continue analysing the case of an optically thin layer in which τ_ν is

very small (or k_ν very small); the equation of transfer is

$$\frac{\mathrm{d}I_\nu}{\mathrm{d}s} = j_\nu \zeta. \tag{35}$$

The integration of the above equation gives

$$I_\nu(s_1) = I_\nu(s_0) + \int_{s_0}^{s_1} j_\nu \zeta \mathrm{d}s. \tag{36}$$

If the background is assumed to be dark, the image is proportional to the integral of the emissivity

$$I_\nu(s_1) = \int_{s_0}^{s_1} j_\nu \zeta \mathrm{d}s. \tag{37}$$

The discrete version of the above equation is

$$I_\nu \propto \sum_1^n \zeta(s) \Delta s, \tag{38}$$

where n is the number of elements belonging to the considered region. The point of view of the observer plays a significant role and we analyse three cases:

1) The Galaxy is seen face on, see **Figure 12** where a theoretical annulus is visible

2) The Galaxy is seen edge on

3) Whole sky map in Hammer-Aitoff or Mollweide projection, see **Figure 13**.

Another interesting astrophysical feature is the annulus with enhanced synchrotron emission, whose distance from the galactic centre lies between 5.5 kpc and 7.6 kpc [30]. In **Figure 14** we isolate a given region of simulated synchrotron emission.

Before continuing, we introduce the simplest model for the image of a spiral galaxy as seen edge on. We assume that the number density C of the radiation-emitting material is constant in a thin cylinder (radius a_s, height h, $h \ll a_s$) and then falls to 0. The line of sight, when the observer is situated at the infinity of the x-axis, is the locus parallel to the x-axis which crosses the position y in a Cartesian x-y plane and terminates at the external circle of radius a_s, see [36]. The length of this locus is

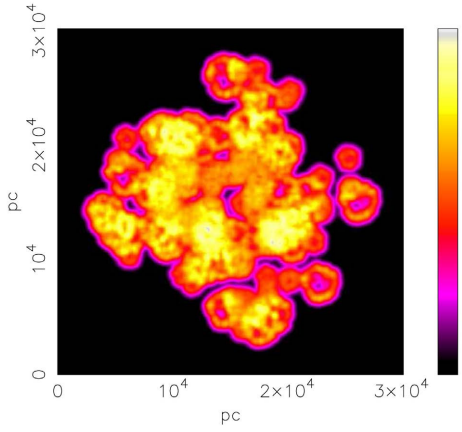

Figure 12. Intensity of synchrotron emission when the galaxy is face on, see parameters of the diffusion in **Table 5**.

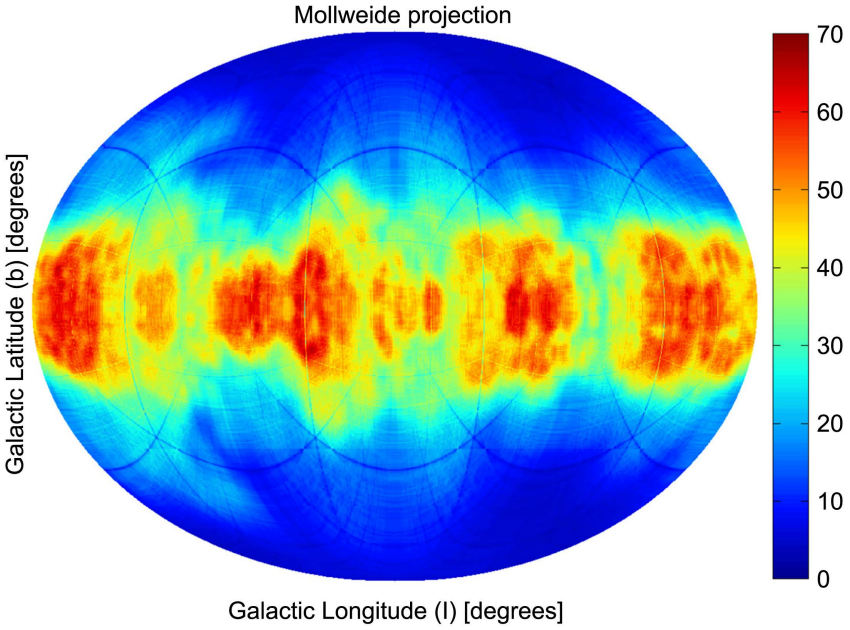

Figure 13. Intensity of synchrotron emission when the Galaxy is seen in Mollweide projection, see parameters of the diffusion in **Table 5**.

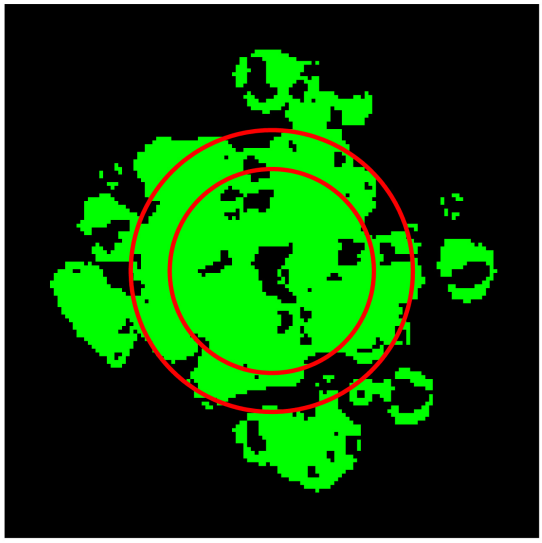

Figure 14. Intensity map of synchrotron emission comprised between the maximum and maximum/2.1 (green zone), which has the appearance of an irregular annulus, and two radii, 5.5 kpc and 7.6 kpc (red circles) which include the observed annulus; parameters as in **Figure 12**.

$$l_{0a_s} = 2 \times \sqrt{a_s^2 - y^2}; \quad 0 \le y < a_s. \tag{39}$$

The number density C_m is constant in the thin cylinder of radius a_s and therefore the intensity of the radiation is

$$I_{0a_s} \propto C_m \times 2 \times \sqrt{a^2 - y^2} \propto C_m \times 2a_s \sin(\theta); \quad 0 \le y < a_s, \tag{40}$$

where the angle θ varies between −90 deg and 90 deg. An example of the

Galaxy as seen edge on is given by the radio emission at 408 MHz as detected by Planck which is reported in Figure 5 of [22], see **Figure 15**. We now analyse whether the sine law as represented by the above equation is comparable with standard fits. For this purpose **Figure 16** reports the comparison of the radio-intensity versus galactic longitude with the sine law, a polynomial fit and a Gaussian fit; the χ^2 being evaluated in **Table 6**.

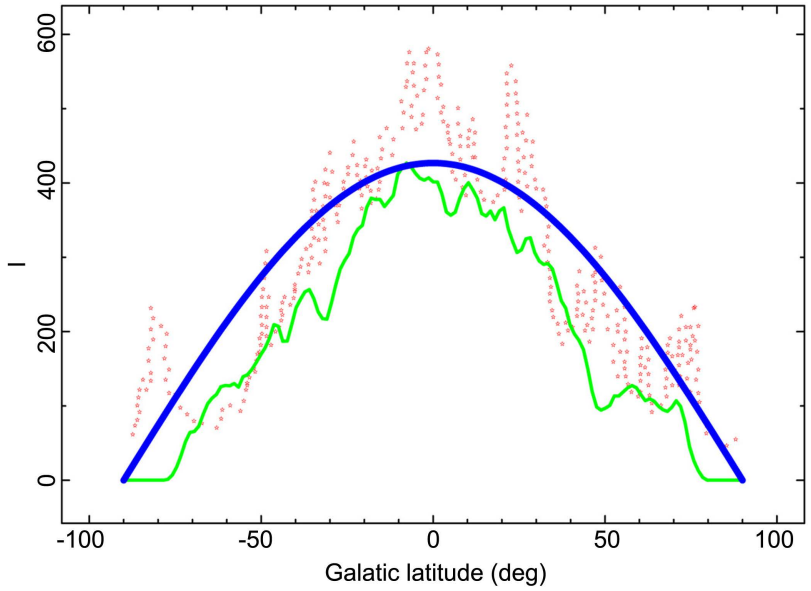

Figure 15. Intensity of synchrotron emission in Mollweide projection, see parameters of the diffusion in **Table 5** (green line), observed data as in Figure 5 of [22] (red points) and blue theoretical thick line given by the trigonometrical Equation (40).

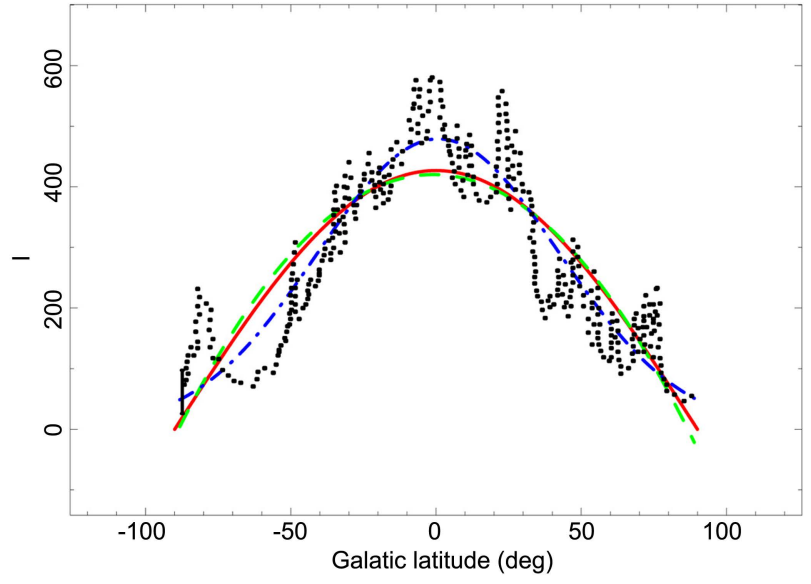

Figure 16. Observed intensity of synchrotron emission in Mollweide projection, as in Figure 5 of [22] (black points), red theoretical thick line given by the trigonometrical Equation (40), the green dashed line represents the polynomial approximation and the blue dash-dot-dash the Gaussian approximation.

6.6. The Spectral Index

Let us assume that the initial number of CRs that are diffusing, N, has the following dependence on the diffusion coefficient:

$$N = N_0 \left(D/D_0 \right)^{\beta}, \tag{41}$$

where β is the exponent of the power law. The analytical solution to the transient equation of diffusion with losses, Equation (15), for an initial $\sin^4$ profile of concentration is

$$u(x,t) = \frac{N_0 \left(\frac{D}{D_0} \right)^{\beta} \left(\cos\left(\frac{4\pi x}{L} \right) \mathrm{e}^{-\frac{t\left(16D\pi^2 + L^2 a_l\right)}{L^2}} - 4\cos\left(\frac{2\pi x}{L} \right) \mathrm{e}^{-\frac{t\left(4D\pi^2 + L^2 a_l\right)}{L^2}} + 3\mathrm{e}^{-a_l t} \right)}{8}. \tag{42}$$

In the above equation the diffusion coefficient can be expressed in terms of energy in GeV, see Equation (7), by Table 7.

$$u(x,t) = \left(\frac{E(\mathrm{GeV})}{E_0(\mathrm{GeV})} \right)^{\beta} \times \left(0.125 N_0 \mathrm{e}^{-\frac{1.0\times10^{-14} t\left(1.0\times10^{14} L^2 a_l + 2.611\times10^{9} E(\mathrm{GeV})\right)}{L^2}} \cos\left(\frac{12.566x}{L} \right) \right.$$
$$\left. - 0.5 N_0 \mathrm{e}^{-\frac{8.0\times10^{-15} t\left(1.25\times10^{14} L^2 a_l + 8.162\times10^{8} E(\mathrm{GeV})\right)}{L^2}} \cos\left(\frac{6.283x}{L} \right) + 0.37 N_0 \mathrm{e}^{-1.0 a_l t} \right). \tag{43}$$

Figure 17 reports the results of the simulation of CRs as well the data for CRs as extracted from [37].

Table 6. Numerical values of the parameters for the χ^2 as given by Equation (22) for distribution of radio-emission versus longitude.

Case	Reference	χ^2, Sine model	χ^2, Polynomial profile	χ^2, Gaussian profile
radio-observations	[22]	1,900,888	2,130,949	1,192,361
simulation	this paper	1,384,459	1,005,467	1,192,579

Table 7. Numerical values of the parameters for the transient diffusion with losses computed with Equation (43).

$L = 2000$ pc
$x = 500$ pc
$N_0 = 5 \times 10^8$
$t = 3 \times 10^7$ year
$a_l = 10^{-7}$/year
$E_0 = 10$ GeV
$\beta = -3$

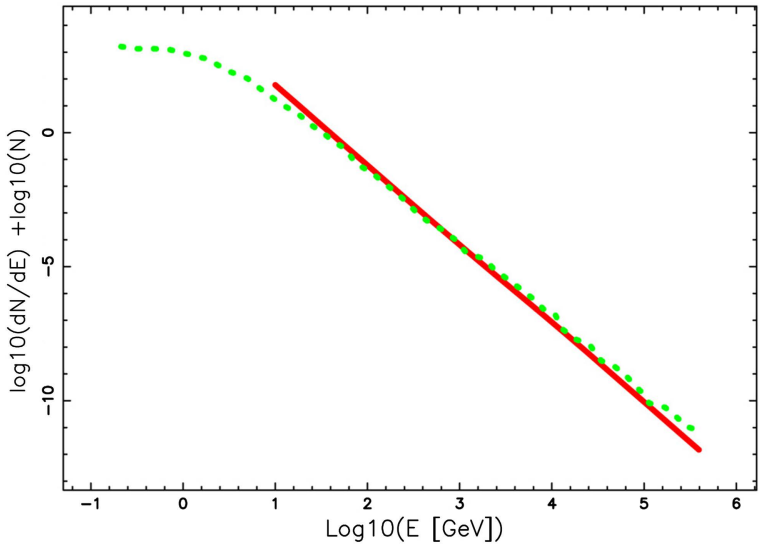

Figure 17. Flux of Hydrogen versus energy per nucleus in Gev: experimental data (green points) and theoretical power law (red full line) as given by Formula (43) with parameters as in Table 7.

7. Conclusions

Diffusion with Stationary State

A new solution for the 1D diffusion equation with losses proportional to the concentration was derived, see Equations (13) and (14).

PDE & Boundary Conditions

Two new solutions for the transient 1D diffusion with losses in terms of Fourier series were derived. The *first* solution is in the presence of an exponential profile of concentration, see Equation (17), and the *second* solution was derived in the presence of a trigonometric profile, see Equation (19). A *third* analytical solution was derived in the case on an initial $\sin^4$ profile of concentration, see Equation (21).

The Astrophysical Profiles

The new laws derived for the diffusion of CRs were applied to the observed profiles of radiation versus galactic latitude, analysing two cases of diffuse γ-ray emission, see Figure 6 and Figure 7, and one case of radio emission, see Figure 8. The analysis of the χ^2 as reported in Table 1 suggests that in one of the three cases considered the analysed new physical mechanisms produces a χ^2 smaller than for the polynomial and the Gaussian fits. A longitude distribution of emission at 408 Mhz along the galactic plane as well the theoretical profile were reported in Figure 15. An analysis of the χ^2 for the observed radio-case indicates that the sine law given by Equation (40) produces a χ^2 smaller than the polynomial fit but bigger than the Gaussian fit, see first line of Table 6. In the simulated case the χ^2 is comparable but bigger than the polynomial and Gaussian fit, see the second line in Table 6. In other words we have validated a classical explanation for the excess of radiation observed in the various astronomical bands at the centre of the galaxy.

The Astrophysical Map

Figure 12 reports a map of the theoretical synchrotron emission for a spiral galaxy as seen face on. The tendency to form an annulus, such as that reported in Figure 2 in [30], is due to the combination of the spiral structure with the diffusion of CRs.

Future Projects

The arguments here developed can be applied to the analysis of the γ-ray background, following the hypothesis that it is produced by the star-forming galaxies [38]. The SBs are hot and emit X-rays, so there are a lot of electrons for the gamma-rays to scatter and therefore the hypothesis of the inverse Compton production of radiation should be considered.

Conflicts of Interest

The author declares no conflicts of interest regarding the publication of this paper.

References

[1] Streimatter, R.E., Balasubrahmanyan, V.K., Protheroe, R.J. and Ormes, J.F. (1985) Cosmic Ray Propagation in the Local Superbubble. *Astronomy & Astrophysics*, **143**, 249-255.

[2] Higdon, J.C., Lingenfelter, R.E. and Ramaty, R. (1998) Cosmic-Ray Acceleration from Supernova Ejecta in Superbubbles. *The Astrophysical Journal*, **509**, L33-L36. https://doi.org/10.1086/311757

[3] Alibés, A., Labay, J. and Canal, R. (2002) Galactic Cosmic Rays from Superbubbles and the Abundances of Lithium, Beryllium, and Boron. *The Astrophysical Journal*, **571**, 326-333. (Preprint) https://doi.org/10.1086/339937

[4] Higdon, J.C. and Lingenfelter, R.E. (2003) The Superbubble Origin of ^{22}Ne in Cosmic Rays. *The Astrophysical Journal*, **590**, 822-832. https://doi.org/10.1086/375192

[5] Higdon, J.C. and Lingenfelter, R.E. (2005) OB Associations, Supernova-Generated Superbubbles, and the Source of Cosmic Rays. *The Astrophysical Journal*, **628**, 738-749. https://doi.org/10.1086/430814

[6] Lingenfelter, R.E. and Higdon, J.C. (2007) Cosmic Rays, Dust, and the Mixing of Supernova Ejecta into the Interstellar Medium in Superbubbles. *The Astrophysical Journal*, **660**, 330-335. https://doi.org/10.1086/513420

[7] Butt, Y.M. and Bykov, A.M. (2008) A Cosmic-Ray Resolution to the Superbubble Energy Crisis. *The Astrophysical Journal*, **677**, L21-L22. (Preprint) https://doi.org/10.1086/587875

[8] Ferrand, G. and Marcowith, A. (2010) On the Shape of the Spectrum of Cosmic Rays Accelerated Inside Superbubbles. *Astronomy & Astrophysics*, **510**, Article No. A101. (Preprint) https://doi.org/10.1051/0004-6361/200913520

[9] Barghouty, A.F. and Schnee, D.A. (2012) Anomalous Transport of High-energy Cosmic Rays in Galactic Superbubbles. I. Numerical Simulations. *The Astrophysical Journal*, **749**, 178-188. https://doi.org/10.1088/0004-637X/749/2/178

[10] Heesen, V., Brinks, E., Krause, M.G.H., Harwood, J.J., Rau, U., Rupen, M.P., Hunter, D.A., Chyży, K.T. and Kitchener, G. (2015) The Non-Thermal Superbubble in IC

10: The Generation of Cosmic Ray Electrons Caught in the Act. *Monthly Notices of the Royal Astronomical Society*: *Letters*, **447**, L1-L5. (Preprint) https://doi.org/10.1093/mnrasl/slu168

[11] Gupta, S., Nath, B.B., Sharma, P. and Eichler, D. (2018) Lack of Thermal Energy in Superbubbles: Hint of Cosmic Rays? *Monthly Notices of the Royal Astronomical Society*: *Letters*, **473**, 1537-1553. (Preprint) https://doi.org/10.1093/mnras/stx2427

[12] Lingenfelter, R.E. (2018) Cosmic Rays from Supernova Remnants and Superbubbles. *Advances in Space Research*, **62**, 2750-2763. (Preprint) https://doi.org/10.1016/j.asr.2017.04.006

[13] Tolksdorf, T., Grenier, I.A., Joubaud, T. and Schlickeiser, R. (2019) Cosmic Rays in Superbubbles. *The Astrophysical Journal*, **879**, 66-76. https://doi.org/10.3847/1538-4357/ab24c6

[14] Zhang, Z., Murase, K. and Mészáros, P. (2020) Cosmic Rays Escaping from Galactic Starburst-Driven Superbubbles. *Monthly Notices of the Royal Astronomical Society*: *Letters*, **492**, 2250-2260. (Preprint) https://doi.org/10.1093/mnras/staa022

[15] Joubaud, T., Grenier, I.A., Casandjian, J.M., Tolksdorf, T. and Schlickeiser, R. (2020) The Cosmic-Ray Content of the Orion-Eridanus Superbubble. *Astronomy & Astrophysics*, **635**, Article No. A96. (Preprint) https://doi.org/10.1051/0004-6361/201937205

[16] Vieu, T., Gabici, S., Tatischeff, V. and Ravikularaman, S. (2022) Cosmic Ray Production in Superbubbles. *Monthly Notices of the Royal Astronomical Society*: *Letters*, **512**, 1275-12293. (Preprint) https://doi.org/10.1093/mnras/stac543

[17] Murgia, S. (2020) The Fermi-LAT Galactic Center Excess: Evidence of Annihilating Dark Matter? *Annual Review of Nuclear and Particle Science*, **70**, 455-483. https://doi.org/10.1146/annurev-nucl-101916-123029

[18] Gould, H. and Tobochnik, J. (1988) An Introduction to Computer Simulation Methods. Addison-Wesley, Reading, MA.

[19] Press, W.H., Teukolsky, S.A., Vetterling, W.T. and Flannery, B.P. (1992) Numerical Recipes in Fortran 77. The Art of Scientific Computing. Cambridge University Press, Cambridge.

[20] Abdo, A.A., Allen, B., Aune, T., *et al.* (2008) A Measurement of the Spatial Distribution of Diffuse TeV Gamma-Ray Emission from the Galactic Plane with Milagro. *The Astrophysical Journal*, **688**, 1078-1083. (Preprint)

[21] Bartoli, B., Bernardini, P., Bi, X.J., *et al.* (2015) Study of the Diffuse Gamma-Ray Emission from the Galactic Plane with ARGO-YBJ. *The Astrophysical Journal*, **806**, 20-31. (Preprint)

[22] Planck Collaboration, P.A.R.A., Aghanim, N., Alves, M.I.R., *et al.* (2015) Planck Intermediate Results. XXIII. Galactic Plane Emission Components Derived from Planck with Ancillary Data. *Astronomy & Astrophysics*, **580**, A13-A41. (Preprint)

[23] Seiden, P.E. and Gerola, H. (1979) Properties of Spiral Galaxies from a Stochastic Star Formation Model. *The Astrophysical Journal*, **233**, 56-66. https://doi.org/10.1086/157366

[24] Seiden, P.E. (1983) The Role of the Gas in Propagating Star Formation. *The Astrophysical Journal*, **266**, 555-561. https://doi.org/10.1086/157366

[25] Schulman, L.S. and Seiden, P.E. (1986) Percolation and Galaxies *Science*, **233**, 425-431. https://doi.org/10.1126/science.233.4762.425

[26] Zaninetti, L. (1988) Percolation and Synchrotron Emission. I—The Case of Spiral Galaxies. *Astronomy & Astrophysics*, **190**, 17-20.

[27] Seiden, P.E. and Schulman, L.S. (1990) Percolation Model of Galactic Structure. *Advances in Physics*, **39**, 1-54. https://doi.org/10.1080/00018739000101461

[28] Zaninetti, L. (2017) The Milky Way as Modeled by Percolation and Superbubbles. (Preprint)

[29] Jungwiert, B. and Palouš, J. (1994) Stochastic Self-Propagating Star Formation with Anisotropic Probability Distribution. *Astronomy & Astrophysics*, **287**, 55-67.

[30] Vallée, J.P. (2022) Superposing the Magnetic Spiral Structure of the Milky Way, on the Stellar Spiral Arms—Matching the Unique Galactic Magnetic Field Reversal Zone with Two Galactic Spiral Arm Segments. *International Journal of Astronomy and Astrophysics*, **12**, 281-300. https://doi.org/10.4236/ijaa.2022.124017

[31] Bisnovatyi-Kogan, G.S. and Silich, S.A. (1995) Shock-Wave Propagation in the Non-uniform Interstellar Medium. *Reviews of Modern Physics*, **67**, 661-712. https://doi.org/10.1103/RevModPhys.67.661

[32] Dickey, J.M. and Lockman, F.J. (1990) H I in the Galaxy. *Annual Review of Astronomy and Astrophysics*, **28**, 215-259. https://doi.org/10.1146/annurev.aa.28.090190.001243

[33] Lockman, F.J. (1984) The H I Halo in the Inner Galaxy. *The Astrophysical Journal*, **283**, 90-97. https://doi.org/10.1086/162277

[34] Rybicki, G. and Lightman, A. (1991) Radiative Processes in Astrophysics. Wiley-Interscience, New York.

[35] Hjellming, R.M. (1988) Radio Stars. In: Verschuur, G.L. and Kellermann, K.I., Eds., *Galactic and Extragalactic Radio Astronomy*, *Astronomy and Astrophysics Library*, Springer-Verlag, Berlin, 381-438. https://doi.org/10.1007/978-1-4612-3936-9_9

[36] Zaninetti, L. (2009) Scaling for the Intensity of Radiation in Spherical and Aspherical Planetary Nebulae. *Monthly Notices of the Royal Astronomical Society*: *Letters*, **395**, 667-697. https://doi.org/10.1111/j.1365-2966.2009.14551.x

[37] Zyla, P., *et al.* (Particle Data Group) (2020) Review of Particle Physics. *PTEP*: *Progress of Theoretical and Experimental Physics*, **2020**, 083C01.

[38] Roth, M.A., Krumholz, M.R., Crocker, R.M. and Celli, S. (2021) The Diffuse γ-Ray Background Is Dominated by Star-Forming Galaxies. *Nature*, **597**, 341-344. (Preprint) https://doi.org/10.1038/s41586-021-03802-x

Appendix: Solution of the ODE

The ODE of the second order

$$D\left(\frac{\mathrm{d}^2}{\mathrm{d}x^2}u(x)\right)-a_l u(x)=0, \tag{A.1}$$

is homogeneous and has constant coefficients. A trial solution is

$$u(x)=\mathrm{e}^{rx}, \tag{A.2}$$

the characteristic polynomial is

$$Dr^2-a_l=0, \tag{A.3}$$

which has roots

$$r_1=\frac{\sqrt{a_l}}{\sqrt{D}},\quad r_2=-\frac{\sqrt{a_l}}{\sqrt{D}}. \tag{A.4}$$

The general solution of the ODE is

$$u(x)=c_1\mathrm{e}^{\frac{\sqrt{a_l}x}{\sqrt{DD}}}+c_2\mathrm{e}^{-\frac{\sqrt{a_l}x}{\sqrt{DD}}}. \tag{A.5}$$

We now introduce two boundary conditions $u(a)=0$ and $u(b)=C_m$ which yields a system of two equations in the two variables c_1 and c_2

$$c_1\mathrm{e}^{\frac{\sqrt{a_l}a}{\sqrt{D}}}+c_2\mathrm{e}^{-\frac{\sqrt{a_l}a}{\sqrt{D}}}=0, \tag{A.6a}$$

$$c_1\mathrm{e}^{\frac{\sqrt{a_l}b}{\sqrt{D}}}+c_2\mathrm{e}^{-\frac{\sqrt{a_l}b}{\sqrt{D}}}=C_m. \tag{A.6b}$$

The two solutions of the system are

$$c_1=-\frac{C_m\mathrm{e}^{-\frac{\sqrt{a_l}a}{\sqrt{D}}}}{-\mathrm{e}^{-\frac{\sqrt{a_l}a}{\sqrt{D}}}\mathrm{e}^{\frac{\sqrt{a_l}b}{\sqrt{D}}}+\mathrm{e}^{-\frac{\sqrt{a_l}b}{\sqrt{D}}}\mathrm{e}^{\frac{\sqrt{a_l}a}{\sqrt{D}}}}, \tag{A.7a}$$

$$c_2=\frac{C_m\mathrm{e}^{\frac{\sqrt{a_l}a}{\sqrt{D}}}}{-\mathrm{e}^{-\frac{\sqrt{a_l}a}{\sqrt{D}}}\mathrm{e}^{\frac{\sqrt{a_l}b}{\sqrt{D}}}+\mathrm{e}^{-\frac{\sqrt{a_l}b}{\sqrt{D}}}\mathrm{e}^{\frac{\sqrt{a_l}a}{\sqrt{D}}}}, \tag{A.7b}$$

and therefore the solution of the ODE is

$$u(x)=\frac{C_m\left(\mathrm{e}^{\frac{2\sqrt{a_l}(a-x)}{\sqrt{D}}}-1\right)\mathrm{e}^{-\frac{\sqrt{a_l}(b-x)}{\sqrt{D}}}}{\mathrm{e}^{\frac{2\sqrt{a_l}(a-b)}{\sqrt{D}}}-1}. \tag{A.8}$$